Imprints of gravitational-wave polarizations on projected tidal tensor in three dimensions

Yusuke Mikura,[*,1] Teppei Okumura,[*,†,2] Misao Sasaki[†‡§$,3]

* Institute of Astronomy and Astrophysics, Academia Sinica,
  No. 1, Section 4, Roosevelt Road, Taipei 10617, Taiwan
† Kavli Institute for the Physics and Mathematics of the Universe (WPI), UTIAS,
  The University of Tokyo, Kashiwa, Chiba 277-8583, Japan
‡ Asia Pacific Center for Theoretical Physics (APCTP),
  Pohang 37673, Korea
§ Center for Gravitational Physics, Yukawa Institute for Theoretical Physics,
  Kyoto University, Kyoto 606-8502, Japan
$ Leung Center for Cosmology and Particle Astrophysics,
  National Taiwan University, Taipei 10617, Taiwan

Abstract: Gravitational waves (GWs) distort galaxy shapes through the tidal effect, offering a novel avenue to probe the nature of gravity. In this paper, we investigate how extra GW polarizations beyond those predicted by general relativity imprint observable signatures on galaxy shapes. Since galaxy shapes are measured as two-dimensional images projected onto the celestial sphere, we present three-dimensional statistical quantities of the projected tidal tensor sourced by the tensor perturbation. We show that the presence of extra polarization modes modifies both the amplitude and angular dependence of the correlation functions. Furthermore, we identify a distinct observational channel for probing parity violation in helicity-two and helicity-one modes. In particular, we show that if they propagate at different speeds, galaxy surveys can disentangle the source of parity violation. Our findings establish a theoretical framework for using upcoming large-scale galaxy surveys to test modified gravity theories through the polarization content of GWs.

[1] ymikura@asiaa.sinica.edu.tw
[2] tokumura@asiaa.sinica.edu.tw
[3] misao.sasaki@ipmu.jp

Contents

1   Introduction

The detection of gravitational waves (GWs) by the LIGO-Virgo Collaboration has opened a new era of cosmology where we can probe fundamental physics through GWs [1–5]. There are many mechanisms that can generate a stochastic GW background over a huge range of frequencies, and appropriate ways to search for the signals vary depending on the frequency of interest. The lowest frequency band accessible to us spans approximately from 10^{-20} Hz to 10^{-16} Hz, where GWs originate in the vacuum fluctuations during inflation. This frequency range can be probed by the B-mode signal in the polarization of the cosmic microwave background, and it has been a central topic in observational cosmology for decades. Other than that, there exist several GW observatories searching for signals with frequencies ranging from 10^{-9} Hz to 10^4 Hz. For instance, ground-based observatories probe the high-frequency GWs ranging from 10 Hz-10^4 Hz [6–9] and space-based detectors will observe GWs with frequencies between 10^{-4} Hz and 10^{-1} Hz [10, 11]. It is also beneficial to utilize pulsar timing arrays (PTA) to explore the spectrum between 10^{-9} Hz and 10^{-6} Hz, where of particular interest would go to the recent evidence reported by the NANOGrav collaboration [12]. Even with the above-mentioned observatories, there still exists a wide range of window that has not been explored well. Interestingly, some of the frequency windows, roughly around 10^{-16} Hz to 10^{-14} Hz, correspond to the scale of the large-scale structure of the universe, thereby having a potential to be investigated observationally in light of the wealth of upcoming surveys.

There are a variety of ways to extract information about fundamental physics from the large-scale structure. Among several observables, galaxy-shape correlations, referred to as intrinsic alignments (IAs) [13–16], can be beneficial because galaxy shapes are intrinsically aligned with the surrounding environment. Given

that the universe is homogeneous and isotropic on large scales, orientations of galaxies were expected to be random, so that the IAs were first considered as one of the major sources of systematic errors in weak-lensing measurements (see e.g. refs. [17, 18] and references therein). However, it has been recently realized that the IAs themselves have rich information to constrain cosmological parameters, with the large-scale dark matter distribution being a primary example. On large scales, we often adopt the so-called linear alignment model where the intrinsic galaxy shape is assumed to respond linearly to the tidal field generated by the gravitational potential [14, 16, 19, 20]. This model has been confirmed in both simulations and observations [19, 21, 22], implying that the IAs can be indeed an interesting and practical tool to extract cosmological information [23–27]. The amount of cosmological information can be maximized by combining recent theoretical developments [20, 28–34] with measurements of galaxy shapes via imaging observations and of distances to galaxies via spectroscopic observations [20, 35–44].

The origin of the intrinsic shape distortion is not limited to the gravitational potential; it can also be sourced by a rank-two tensor field at leading order [45].[4] This comes from the fact that the tidal force is associated with the perturbed Riemann tensor that is linearly proportional to the tensor perturbation. This idea was generalized to include the effects of the chirality of tensor modes of GWs on angular statistics in ref. [56]. To compare with observations, one has to deal with the linear shape bias for GWs as in the case of the galaxy bias. Ref. [57] tested the ansatz of the linear shape bias used in ref. [45] and confirmed its validity using N-body simulations. Subsequently, this line of research was further extended by examining the auto- and cross-power spectra of the shear E- and B-modes induced by the scalar, vector, and tensor modes in the three-dimensional space [58, 59]. Two of the authors provided in ref. [60] a complementary technique to extract signals of the tensor modes using real-space observables, where a primary quantity is an analogue of the overlap reduction function (ORF) which describes the angular dependence of signals from sources that are spatially separated on the celestial sphere. Ref. [60] showed that, due to the propagation, signals of the tensor modes in the ORF have an oscillatory feature which is absent in ones of the scalar tidal force, making it possible to extract information about the tensor modes out of signals that the scalar tidal force dominates.

In this paper we generalize ref. [60] by including additional scalar and vector components that may appear in metric theories of gravity beyond general relativity (GR) [61, 62]. Classic examples of such include scalar-tensor theories, massive gravity theories, Einstein–Æther theories, and scalar-tensor-vector gravity. Considering upcoming galaxy surveys, it is informative to understand how additional polarization modes affect the analogue of the ORF because it serves as the foundations for fitting some modified-gravity theories with observational data.[5]

The paper is organized as follows. In section 2, we define the polarization tensors and the power spectra of GWs to fix the overall notation. In section 3, we turn to a technique to extract signals of GWs using the projection of a tensor field onto the celestial sphere, presenting general calculations for the power spectra of the traceless projected tensor field. We then investigate the angular- and distance-dependence of an analogue of the ORF with two concrete examples in section 4. Finally, we conclude in section 5. In appendix A, we provide a list of correlations for the projected tensor field without extracting trace. In appendix B, we provide a different way of calculating the analogue of the ORF. Throughout the paper, we adopt the natural unit $c = 1$ and use $\eta_{\mu\nu} = \text{diag}(-1, 1, 1, 1)$ for the sign of the Minkowski metric. A bar denotes a complex conjugate. We use the lowercase Latin alphabet for spacial components in three dimensions and the uppercase Latin alphabet for components in the two-dimensional projected space.

---

[4]The effects of the tensor field on the galaxy clustering and weak lensing have been studied in refs. [46–55].

[5]In PTA, the ORF in GR is known as the Hellings–Downs (HD) curve [63] and, since deviations from the HD curve is a hint of new physics beyond GR, a number of investigations have been made observationally [64] and theoretically [65–68].

2 Power spectra of gravitational waves

We define GWs as the spatial perturbation obtained after imposing the synchronous gauge $h_{0\mu} = 0$ on the tensor perturbation $h_{\mu\nu}$. The line element is then given by[6]

$$ds^2 = a^2(\eta) \left[-d\eta^2 + (\delta_{ij} + h_{ij}) \, dx^i dx^j \right] , \tag{2.1}$$

where a is the scale factor and η is the conformal time. In three-dimensional space, the tensor perturbation h_{ij} can accommodate up to six helicity modes [61,62], that can be labeled by an index $\lambda = \{\pm 2, \pm 1, b, \ell\}$ in the chiral basis. The last two modes have helicity-zero and are called breathing and longitudinal polarizations, respectively. In the Fourier space, the tensor perturbation can be written as

$$h_{ij}(\eta, \boldsymbol{k}) = \sum_\lambda e^{(\lambda)}{}_{ij} h_{(\lambda)}(\eta, \boldsymbol{k}) , \tag{2.2}$$

where the polarization tensors $e^{(\lambda)}{}_{ij}$ are defined as [69]

$$e^{(\pm 2)}{}_{ij} := \frac{1}{2} \left[\left(e^{(1)}{}_i \otimes e^{(1)}{}_j - e^{(2)}{}_i \otimes e^{(2)}{}_j \right) \mp i \left(e^{(1)}{}_i \otimes e^{(2)}{}_j + e^{(2)}{}_i \otimes e^{(1)}{}_j \right) \right] , \tag{2.3}$$

$$e^{(\pm 1)}{}_{ij} := \frac{1}{2} \left[\left(e^{(1)}{}_i \otimes \hat{k}_j + \hat{k}_i \otimes e^{(1)}{}_j \right) \mp i \left(e^{(2)}{}_i \otimes \hat{k}_j + \hat{k}_i \otimes e^{(2)}{}_j \right) \right] , \tag{2.4}$$

$$e^{(b)}{}_{ij} := \frac{1}{\sqrt{2}} \left(e^{(1)}{}_i \otimes e^{(1)}{}_j + e^{(2)}{}_i \otimes e^{(2)}{}_j \right) , \tag{2.5}$$

$$e^{(\ell)}{}_{ij} := \hat{k}_i \otimes \hat{k}_j . \tag{2.6}$$

Here, $\hat{\boldsymbol{k}}$ denotes a unit vector pointing to the propagation of the tensor perturbation, and $\boldsymbol{e}^{(1)}$ and $\boldsymbol{e}^{(2)}$ are two orthonormal vectors. The set of unit vectors $\{\boldsymbol{e}^{(1)}, \boldsymbol{e}^{(2)}, \hat{\boldsymbol{k}}\}$ forms the right-handed Cartesian coordinate system. One can easily show that the above polarizations satisfy

$$e^{(\lambda)}{}_{ij} \bar{e}^{(\lambda')ij} = \delta^{\lambda\lambda'} , \tag{2.7}$$

where the bar denotes the complex conjugate and the polarization tensors with upper indices are the same as those with lower indices, namely $e^{(\lambda)ij} = e^{(\lambda)}{}_{ij}$. We use the Einstein summation convention throughout the paper.

The temporal power spectrum of GWs, $P_h(\eta, \eta', k)$, is defined by the ensemble average as

$$\langle h^{ij}(\eta, \boldsymbol{k}) h_{ij}(\eta', \boldsymbol{k}') \rangle = (2\pi)^3 \, \delta_D^{(3)}(\boldsymbol{k} + \boldsymbol{k}') P_h(\eta, \eta', k) , \tag{2.8}$$

where $\delta_D^{(n)}$ is the n-dimensional Dirac delta function. Under the assumption of an isotropic stochastic GW background, one expects that the cross-power spectra between different helicity modes vanish, thereby giving the following power spectrum for each polarization:

$$\langle h_{(\lambda)}(\eta, \boldsymbol{k}) h_{(\lambda)}(\eta', \boldsymbol{k}') \rangle = (2\pi)^3 \, \delta_D^{(3)}(\boldsymbol{k} + \boldsymbol{k}') \delta_{\lambda\lambda'} P^{(\lambda)}(\eta, \eta', k) . \tag{2.9}$$

For later convenience, let us define tensor- and vector-type power spectra as

$$P^{(\mathrm{T})} := P^{(+2)} + P^{(-2)} , \quad P^{(\mathrm{V})} := P^{(+1)} + P^{(-1)} , \tag{2.10}$$

---

[6]The tidal force distorting galaxy shapes can be described by the geodesic deviation. With the metric (2.1), the tidal field t_{ij} is given by $t_{ij} = \delta R_{i0j0} \simeq \left(h_{ij}'' + \mathcal{H} h_{ij}' \right)$ with $\mathcal{H} := a'/a$ being the conformal Hubble parameter. For modes satisfying $c_\lambda k \gg \mathcal{H}$, we roughly have $t_{ij} \sim c_\lambda^2 k^2 h_{ij}$, which implies that correlations of the tidal field are directly related to those of the tensor perturbation.

with which the total power spectrum $P_h(\eta, \eta', k)$ can be expressed as

$$P_h(\eta, \eta', k) = P^{(\mathrm{T})}(\eta, \eta', k) + P^{(\mathrm{V})}(\eta, \eta', k) + P^{(b)}(\eta, \eta', k) + P^{(\ell)}(\eta, \eta', k) \,. \tag{2.11}$$

For the helicity-two or helicity-one modes, there can be an asymmetry of amplitudes between left- and right-handed waves. To parametrize this chirality, we define tensor- and vector-type chiral parameters $\chi^{(\mathrm{T})}$ and $\chi^{(\mathrm{V})}$ as

$$\chi^{(\mathrm{T})} := \frac{P^{(+2)} - P^{(-2)}}{P^{(\mathrm{T})}} \,, \quad \chi^{(\mathrm{V})} := \frac{P^{(+1)} - P^{(-1)}}{P^{(\mathrm{V})}} \,. \tag{2.12}$$

We next summarize the sub-horizon dynamics of the tensor perturbation. The wave equation for $h_{(\lambda)}(\eta, \boldsymbol{k})$ is given by

$$h''_{(\lambda)} + 2\frac{a'}{a}h'_{(\lambda)} + c_\lambda^2 k^2 h_{(\lambda)} = 0 \,, \tag{2.13}$$

where c_λ is the sound speed of the mode with helicity λ and primes denote derivatives with respect to the conformal time η. Here and hereafter, we assume that the sound speed is nearly constant but can be different from the speed of light. Deep inside the horizon, a solution to the wave equation is given by

$$h_{(\lambda)}(\eta, \boldsymbol{k}) \simeq \frac{a(\eta_{\mathrm{ini}})}{a(\eta)} \left[\cos\left[c_\lambda k(\eta - \eta_{\mathrm{ini}}) + \phi_{\boldsymbol{k}}\right] h_{(\lambda)}(\eta_{\mathrm{ini}}, \boldsymbol{k}) + \frac{1}{c_\lambda k}\sin\left[c_\lambda k(\eta - \eta_{\mathrm{ini}}) + \phi_{\boldsymbol{k}}\right] h'_{(\lambda)}(\eta_{\mathrm{ini}}, \boldsymbol{k}) \right] \,, \tag{2.14}$$

where η_{ini} denotes the conformal time either right after GWs are generated or when the scale entered the horizon if GWs are primordial. The phase $\phi_{\boldsymbol{k}}$ represents the effect of inhomogeneities during propagation from η_{ini} to η. We note that our discussion is applicable to both GWs with primordial origin and ones generated by some other sources. By generation we mean that the GWs are produced by causal sub-horizon mechanisms including astrophysical events and cosmological events such as phase transitions. If GWs are of the primordial origin, they may be phase coherent at first. However, long-distance propagation on the perturbed universe randomizes the phase ϕ_k, allowing us to assume it random [70, 71]. Therefore, in both cases, the power spectrum can be written as

$$P^{(\lambda)}(\eta, \eta', k) \simeq \frac{a^2(\eta_{\mathrm{ini}})}{a(\eta)a(\eta')} \cos\left[c_\lambda k\left(\eta - \eta'\right)\right] P^{(\lambda)}_{\mathrm{ini}}(k) \,, \tag{2.15}$$

where $P^{(\lambda)}_{\mathrm{ini}}(k)$ is the initial power spectrum.

3 Power spectra of projected traceless tensor

Given the fact that galaxy shapes are observed as two-dimensional images from galaxy surveys, we need to introduce correlation functions in three dimensions using the tensor perturbation projected onto the celestial sphere. In this work, we focus on its trace-free part with an expectation that its trace part cannot be easily evaluated in the presence of an extrinsic (lensing) contribution. In section 3.1, we explain how the tensor perturbation is projected onto the celestial sphere. We then present the power spectra made up with tensors with trace extracted in subsequent sections.[7]

---

[7]See appendix A for the power spectra of the tensor perturbation without extracting trace.

3.1 Projection onto the two-dimensional plane

Let us start with the projection of the tensor perturbation onto a two-dimensional space under the flat-sky approximation. To this end, we write a coordinate system in real space as $\{\hat{\boldsymbol{x}}, \hat{\boldsymbol{y}}, \hat{\boldsymbol{z}}\}$, and choose such that the z-axis points to the line of sight (LOS) and the x-axis is aligned with $\boldsymbol{e}^{(1)}$ which is the orthonormal vector of the system $\{\boldsymbol{e}^{(1)}, \boldsymbol{e}^{(2)}, \hat{\boldsymbol{k}}\}$. In the system $\{\hat{\boldsymbol{x}}, \hat{\boldsymbol{y}}, \hat{\boldsymbol{z}}\}$, the vectors $\boldsymbol{e}^{(1)}$, $\boldsymbol{e}^{(2)}$, and $\hat{\boldsymbol{k}}$ can be expressed as

$$e^{(1)}{}_i = (1, 0, 0) \ , \quad e^{(2)}{}_i = (0, \cos\theta_k, -\sin\theta_k) \ , \quad \hat{k}_i = (0, \sin\theta_k, \cos\theta_k) \ , \tag{3.1}$$

where θ_k is the angle between the propagating direction of GWs and LOS. The two-dimensional space, which we call the projected space, is spanned by the first and second components in the Cartesian coordinate system $\{\hat{\boldsymbol{x}}, \hat{\boldsymbol{y}}\}$. Therefore, components of the orthonormal vectors $\boldsymbol{e}^{(1)}$, $\boldsymbol{e}^{(2)}$, and $\hat{\boldsymbol{k}}$ in the projected space can be obtained by dropping the third component as

$$e^{(1)}{}_A = (1, 0) \ , \quad e^{(2)}{}_A = (0, \cos\theta_k) \ , \quad \hat{k}_A = (0, \sin\theta_k) \ , \tag{3.2}$$

where we use the uppercase Latin alphabet for components in the projected space. With use of the projected components (3.2), the polarization tensors can be written as

$$e^{(\lambda)}{}_{ij} = \begin{pmatrix} e^{(\lambda)}{}_{AB} & e^{(\lambda)}{}_{Az} \\ e^{(\lambda)}{}_{zB} & e^{(\lambda)}{}_{zz} \end{pmatrix} \ , \tag{3.3}$$

with which one can define the projected tensor field as

$$h_{AB}(\eta, \boldsymbol{k}) = \sum_\lambda e^{(\lambda)}{}_{AB} h_{(\lambda)}(\eta, \boldsymbol{k}) \ . \tag{3.4}$$

One can introduce lower rank tensors out of h_{AB}, and we call them projected vector or scalar fields depending on the number of indices. It should be emphasized that we are interested in correlation functions in three dimensions.

The trace part of the projected tensor field can be easily removed as

$$h^{\mathrm{T}}{}_{AB} := h_{AB} - \frac{1}{2}\delta_{AB}h^C{}_C \ , \tag{3.5}$$

where δ_{AB} is the Kronecker delta in two dimensions. Let us take a look at how each component of the traceless tensor (3.5) is related to the mode functions defined in the three-dimensional space. There exist two components in the traceless projected tensor field since it is a symmetric 2×2 matrix

$$h^{\mathrm{T}}{}_{AB}(\eta, \boldsymbol{k}) = \begin{pmatrix} h^{\mathrm{T}}{}_{xx} & h^{\mathrm{T}}{}_{xy} \\ h^{\mathrm{T}}{}_{yx} & -h^{\mathrm{T}}{}_{xx} \end{pmatrix} \ . \tag{3.6}$$

The (x, x) components is given by

$$\begin{aligned} h^{\mathrm{T}}{}_{xx} = \frac{1}{4}\bigg[&\left(1 + \cos^2\theta_k\right)\left(h_{(+2)} + h_{(-2)}\right) + i\sin\left(2\theta_k\right)\left(h_{(+1)} - h_{(-1)}\right) \\ &+ \sqrt{2}\left(1 + \cos^2\theta_k\right)h_{(b)} - 2\sin^2\theta_k h_{(\ell)}\bigg] \ , \end{aligned} \tag{3.7}$$

5

and the off-diagonal component is composed of the helicity-two and helicity-one modes as

$$h^{\mathrm{T}}{}_{xy} = h^{\mathrm{T}}{}_{yx} = \frac{1}{2}\left[-i\cos\theta_k\left(h_{(+2)} - h_{(-2)}\right) + \sin\theta_k\left(h_{(+1)} + h_{(-1)}\right)\right] . \tag{3.8}$$

It is obvious from above expressions that multiplication of the diagonal or off-diagonal components themselves give rise to parity-even power spectra. In other words, if parity violation exists, its signals appear only in power spectra that mix the diagonal and off-diagonal components. To see these, in the following, we explicitly provide a list of power spectra of fields that are constructed from the traceless projected tensor.

3.2 Projected tensor field

The auto correlation of the traceless projected tensor field can be written as

$$\left\langle h^{\mathrm{T}AB}(\eta,\boldsymbol{k})h^{\mathrm{T}}{}_{AB}(\eta',\boldsymbol{k}')\right\rangle = (2\pi)^3\,\delta_D^{(2)}(\boldsymbol{k}+\boldsymbol{k}')F_{hh}^{\mathrm{T}}(\mu_k,\eta,\eta',k) . \tag{3.9}$$

The function $F_{hh}^{\mathrm{T}}(\mu_k,\eta,\eta',k)$ depends on the angle between the propagating direction of GWs and LOS, $\mu_k := \cos\theta_k$, and the power spectra defined in section 2. Its explicit form can be obtained straightforwardly as

$$\begin{aligned}
F_{hh}^{\mathrm{T}}(\mu_k,\eta,\eta',k) = {}& \frac{1}{8}\left(1 + 6\mu_k^2 + \mu_k^4\right)P^{(\mathrm{T})}(\eta,\eta',k) + \frac{1}{2}\left(1 - \mu_k^4\right)P^{(\mathrm{V})}(\eta,\eta',k) \\
& + \frac{1}{4}\left(1 - \mu_k^2\right)^2 P^{(b)}(\eta,\eta',k) + \frac{1}{2}\left(1 - \mu_k^2\right)^2 P^{(\ell)}(\eta,\eta',k) .
\end{aligned} \tag{3.10}$$

We can see from above that this correlation is parity-even, which is as expected since it is obtained as a combination of $\left(h^{\mathrm{T}}{}_{xx}\right)^2$ and $\left(h^{\mathrm{T}}{}_{xy}\right)^2$. We also observe that the breathing and longitudinal modes have the same μ_k-dependence in their coefficients as their polarization tensors satisfy

$$\left|e_{AB}^{(b)} - \frac{1}{2}\delta_{AB}\left(e^{(b)}\right)^C{}_C\right|^2 = \frac{1}{2}\left|e_{AB}^{(\ell)} - \frac{1}{2}\delta_{AB}\left(e^{(\ell)}\right)^C{}_C\right|^2 . \tag{3.11}$$

This holds true as long as we consider projected quantities. However, the breathing and longitudinal modes can have different coefficients if the trace part is taken into account (see appendix A).

3.3 Projected vector field

In addition to the quadrupole moments corresponding to the shear, it may be possible to extract vector quantities from galaxy images [72]. Expecting this, we consider the power spectra constructed with a derivative of the projected tensor field with trace extracted.

Out of the traceless projected tensor, we can define two vectors by

$$V^{\mathrm{T}}{}_A(\eta,\boldsymbol{k}) := ik^B h^{\mathrm{T}}{}_{BA}(\eta,\boldsymbol{k}) = \left(ik\sin\theta_k h^{\mathrm{T}}{}_{yx}, -ik\sin\theta_k h^{\mathrm{T}}{}_{xx}\right) , \tag{3.12}$$

$$\widetilde{V}^{\mathrm{T}}{}_A(\eta,\boldsymbol{k}) := i\epsilon^{BC}k_B h^{\mathrm{T}}{}_{CA}(\eta,\boldsymbol{k}) = \left(ik\sin\theta_k h^{\mathrm{T}}{}_{xx}, ik\sin\theta_k h^{\mathrm{T}}{}_{xy}\right) , \tag{3.13}$$

where ϵ^{BC} is the Levi-Civita symbol in the two-dimensional projected space. We call the latter $\widetilde{V}^{\mathrm{T}}{}_A(\eta,\boldsymbol{k})$ a curl vector. The auto correlations of these two vectors are defined by

$$\left\langle V^{\mathrm{T}A}(\eta,\boldsymbol{k})V^{\mathrm{T}}{}_A(\eta',\boldsymbol{k}')\right\rangle = (2\pi)^3\,\delta_D^{(2)}(\boldsymbol{k}+\boldsymbol{k}')F_{VV}^{\mathrm{T}}(\mu_k,\eta,\eta',k) , \tag{3.14}$$

$$\left\langle \widetilde{V}^{\mathrm{T}A}(\eta,\boldsymbol{k})\widetilde{V}^{\mathrm{T}}{}_A(\eta',\boldsymbol{k}')\right\rangle = (2\pi)^3\,\delta_D^{(2)}(\boldsymbol{k}+\boldsymbol{k}')F_{\widetilde{V}\widetilde{V}}^{\mathrm{T}}(\mu_k,\eta,\eta',k) . \tag{3.15}$$

It is immediate to verify that the two functions F_{VV}^{T} and $F_{\widetilde{V}\widetilde{V}}^{\mathrm{T}}$ are identical as

$$
\begin{aligned}
F_{VV}^{\mathrm{T}}(\mu_k, \eta, \eta', k) =\ & F_{\widetilde{V}\widetilde{V}}^{\mathrm{T}}(\mu_k, \eta, \eta', k) \\
=\ & \frac{1}{16} k^2 \left(1 - \mu_k^2\right) \left(1 + 6\mu_k^2 + \mu_k^4\right) P^{(\mathrm{T})}(\eta, \eta', k) \\
& + \frac{1}{4} k^2 \left(1 - \mu_k^2\right) \left(1 - \mu_k^4\right) P^{(\mathrm{V})}(\eta, \eta', k) \\
& + \frac{1}{8} k^2 \left(1 - \mu_k^2\right)^3 P^{(b)}(\eta, \eta', k) + \frac{1}{4} k^2 \left(1 - \mu_k^2\right)^3 P^{(\ell)}(\eta, \eta', k) \,,
\end{aligned}
\tag{3.16}
$$

which is parity-even as evidenced by eq. (3.12) and eq. (3.13). Besides, by comparing with eq. (3.10), we see that the following holds true:

$$
\left\langle V^{\mathrm{T}A}(\eta, \boldsymbol{k}) V^{\mathrm{T}}{}_A(\eta', \boldsymbol{k}') \right\rangle = \frac{1}{2} k^2 \left(1 - \mu_k^2\right) \left\langle h^{\mathrm{T}AB}(\eta, \boldsymbol{k}) h^{\mathrm{T}}{}_{AB}(\eta', \boldsymbol{k}') \right\rangle \,.
\tag{3.17}
$$

In order to see parity-violating signals, it is necessary to consider correlations that mix diagonal and off-diagonal components of the matrix (3.6). The cross correlation between the vector and curl vector accomplishes this, whose power spectrum is defined as

$$
\left\langle \widetilde{V}^{\mathrm{T}A}(\eta, \boldsymbol{k}) V^{\mathrm{T}}{}_A(\eta', \boldsymbol{k}') \right\rangle = (2\pi)^3 \, \delta_D^{(2)}(\boldsymbol{k} + \boldsymbol{k}') F_{\widetilde{V}V}^{\mathrm{T}}(\mu_k, \eta, \eta', k) \,,
\tag{3.18}
$$

with

$$
F_{\widetilde{V}V}^{\mathrm{T}} = -\frac{i}{4} k^2 \mu_k \left(1 - \mu_k^4\right) \chi^{(\mathrm{T})} P^{(\mathrm{T})}(\eta, \eta', k) - \frac{i}{2} k^2 \mu_k \left(1 - \mu_k^2\right)^2 \chi^{(\mathrm{V})} P^{(\mathrm{V})}(\eta, \eta', k) \,.
\tag{3.19}
$$

We note that the same expression (3.19) can be obtained if we define two vectors without extracting trace from the projected tensor field, which means

$$
\left\langle \widetilde{V}^{\mathrm{T}A}(\eta, \boldsymbol{k}) V^{\mathrm{T}}{}_A(\eta', \boldsymbol{k}') \right\rangle = \left\langle \widetilde{V}^{A}(\eta, \boldsymbol{k}) V_A(\eta', \boldsymbol{k}') \right\rangle \,,
\tag{3.20}
$$

with

$$
V_A(\eta, \boldsymbol{k}) := ik^B h_{BA}(\eta, \boldsymbol{k}) \,, \quad \widetilde{V}_A(\eta, \boldsymbol{k}) := i\epsilon^{BC} k_B h_{CA}(\eta, \boldsymbol{k}) \,.
\tag{3.21}
$$

3.4 Projected scalar field

For comprehensiveness, let us finally look at the traceless scalar correlations. Using the traceless property of $h^{\mathrm{T}}{}_{AB}$, one can define two scalar quantities as

$$
S^{\mathrm{T}}(\eta, \boldsymbol{k}) := -k^A k^B h^{\mathrm{T}}{}_{AB}(\eta, \boldsymbol{k}) = k^2 \sin^2 \theta_k h^{\mathrm{T}}{}_{xx} \,,
\tag{3.22}
$$

$$
\widetilde{S}^{\mathrm{T}}(\eta, \boldsymbol{k}) := -\epsilon^{AC} k_C k^B h^{\mathrm{T}}{}_{AB}(\eta, \boldsymbol{k}) = -k^2 \sin^2 \theta_k h^{\mathrm{T}}{}_{xy} \,,
\tag{3.23}
$$

where we call the second a curl scalar. The definitions of the two scalars imply that their auto correlations are parity-even and their cross correlation can lead to parity-violating signals. The auto correlation of the scalar becomes

$$
\left\langle S^{\mathrm{T}}(\eta, \boldsymbol{k}) S^{\mathrm{T}}(\eta', \boldsymbol{k}') \right\rangle = (2\pi)^3 \, \delta_D^{(2)}(\boldsymbol{k} + \boldsymbol{k}') F_{SS}^{\mathrm{T}}(\mu_k, \eta, \eta', k) \,,
\tag{3.24}
$$

with

$$F_{SS}^{\mathrm{T}}(\mu_k, \eta, \eta', k) = \frac{1}{16} k^4 \left(1 - \mu_k^4\right)^2 P^{(\mathrm{T})}(\eta, \eta', k) + \frac{1}{4} k^4 \mu_k^2 \left(1 - \mu_k^2\right)^3 P^{(\mathrm{V})}(\eta, \eta', k)$$
$$+ \frac{1}{8} k^4 \left(1 - \mu_k^2\right)^4 P^{(b)}(\eta, \eta', k) + \frac{1}{4} k^4 \left(1 - \mu_k^2\right)^4 P^{(\ell)}(\eta, \eta', k) , \tag{3.25}$$

while one of the curl scalar is given by

$$\left\langle \widetilde{S}^{\mathrm{T}}(\eta, \boldsymbol{k}) \widetilde{S}^{\mathrm{T}}(\eta', \boldsymbol{k}') \right\rangle = (2\pi)^3 \delta_D^{(2)}(\boldsymbol{k} + \boldsymbol{k}') F_{\widetilde{S}\widetilde{S}}^{\mathrm{T}}(\mu_k, \eta, \eta', k) , \tag{3.26}$$

with

$$F_{\widetilde{S}\widetilde{S}}^{\mathrm{T}}(\mu_k, \eta, \eta', k) = \frac{1}{4} k^4 \mu_k^2 \left(1 - \mu_k^2\right)^2 P^{(\mathrm{T})}(\eta, \eta', k) + \frac{1}{4} k^4 \left(1 - \mu_k^2\right)^3 P^{(\mathrm{V})}(\eta, \eta', k) . \tag{3.27}$$

Finally, the cross correlation of the standard scalar and curl scalar is expressed as

$$\left\langle \widetilde{S}^{\mathrm{T}}(\eta, \boldsymbol{k}) S^{\mathrm{T}}(\eta', \boldsymbol{k}') \right\rangle = (2\pi)^3 \delta_D^{(2)}(\boldsymbol{k} + \boldsymbol{k}') F_{\widetilde{S}S}^{\mathrm{T}}(\mu_k, \eta, \eta', k) , \tag{3.28}$$

where the explicit form of the function $F_{\widetilde{S}S}^{\mathrm{T}}$ is given by

$$F_{\widetilde{S}S}^{\mathrm{T}}(\mu_k, \eta, \eta', k) = -\frac{i}{8} k^4 \mu_k \left(1 - \mu_k^2\right)^2 \left(1 + \mu_k^2\right) \chi^{(\mathrm{T})} P^{(\mathrm{T})}(\eta, \eta', k)$$
$$- \frac{i}{4} k^4 \mu_k \left(1 - \mu_k^2\right)^3 \chi^{(\mathrm{V})} P^{(\mathrm{V})}(\eta, \eta', k) . \tag{3.29}$$

We note that this function is related to the vector cross-correlation as

$$F_{\widetilde{S}S}^{\mathrm{T}} = \frac{1}{2} k^2 \left(1 - \mu_k^2\right) F_{\widetilde{V}V}^{\mathrm{T}} . \tag{3.30}$$

4 The overlap reduction function

We turn to the properties of the two-point correlation functions. We provide our definition of the ORF in section 4.1 and present two concrete examples in section 4.2.

4.1 Definition

Letting X and Y be rank-n tensors such as $h^{\mathrm{T}}{}_{AB}$ and $V^{\mathrm{T}}{}_A$, the two-point correlation function may be written as

$$\left\langle X(\eta, \boldsymbol{x}) Y(\eta', \boldsymbol{x}') \right\rangle = \int \frac{k^2 \mathrm{d}k}{(2\pi)^3} \int \mathrm{d}\Omega_k \left[k^{2(2-n)} \tilde{F}_{XY}(\mu_k, \eta, \eta', k) \mathrm{e}^{i\boldsymbol{k}\cdot(\boldsymbol{x}-\boldsymbol{x}')} \right] , \tag{4.1}$$

where $\tilde{F}_{XY} := F_{XY}/k^{2(2-n)} \propto k^0$ and $\mathrm{d}\Omega_k$ denotes the angular element in the Fourier space.[8] Recalling that the power spectrum with helicity λ is given in eq. (2.15), we can write

$$\tilde{F}_{XY}(\mu_k, \eta, \eta', k) = \sum_\lambda f^{(\lambda)}(\mu_k) P^{(\lambda)}(\eta, \eta', k) ,$$
$$= \frac{a^2(\eta_{\mathrm{ini}})}{a(\eta)a(\eta')} \sum_\lambda \cos \left[c_\lambda k \left(\eta - \eta'\right) \right] f^{(\lambda)}(\mu_k) P_{\mathrm{ini}}^{(\lambda)}(k) . \tag{4.2}$$

---

[8]This expression is no longer true for correlations where the trace of the tensor $g^{AB} h_{AB}$ is involved.

Here, the function $f^{(\lambda)}(\mu_k)$ depends on a specific choice of correlations.

We restrict ourselves to the case where all helicity modes have the same spectral characteristics allowing different amplitudes. Under this assumption, we can parametrize as

$$P_{\text{ini}}^{(\lambda)}(k) = N^{(\lambda)} P_{h,\text{ini}}(k) \,, \tag{4.3}$$

with a condition

$$\sum_\lambda N^{(\lambda)} = 1 \,. \tag{4.4}$$

This assumption enables us to factorize the two-point function as

$$\langle X(\eta, \boldsymbol{x}) Y(\eta', \boldsymbol{x}') \rangle = \frac{a^2(\eta_{\text{ini}})}{a(\eta)a(\eta')} \int \frac{k^{2(3-n)}\mathrm{d}k}{(2\pi)^3} \Gamma_{XY} P_{h,\text{ini}}(k) \,, \tag{4.5}$$

where Γ_{XY} is given by

$$\Gamma_{XY} := \int \mathrm{d}\Omega_k \hat{\Gamma}_{XY} \mathrm{e}^{i\boldsymbol{k}\cdot(\boldsymbol{x}-\boldsymbol{x}')} \,, \tag{4.6}$$

with

$$\hat{\Gamma}_{XY} := \sum_\lambda \cos\left[c_\lambda k \left(\eta - \eta'\right)\right] f^{(\lambda)}(\mu_k) N^{(\lambda)} \,. \tag{4.7}$$

We call the kernel Γ_{XY} an ORF following the terminology used in the PTA.

In order to analyze eq. (4.6), we adopt the flat-sky approximation and choose the coordinate system in the real space as

$$x'^\mu = \left(\eta', 0, 0, r'\right) \,, \quad x^\mu = (\eta, r\sin\theta\cos\theta, r\sin\theta\sin\theta, r\cos\theta) \,, \tag{4.8}$$

meaning that we take the LOS direction to point toward a galaxy at $\boldsymbol{x}'$ and consider that another galaxy is located at a point $\boldsymbol{x}$. The wavevector can point to arbitrary directions, so that we take

$$\boldsymbol{k} = (k\sin\theta_k\cos\theta_k, k\sin\theta_k\sin\theta_k, k\cos\theta_k) \,. \tag{4.9}$$

The angular integral of eq. (4.6) can be performed by means of the spherical harmonics expansion.[9] Letting $\boldsymbol{R} = \boldsymbol{x} - \boldsymbol{x}'$ be a separation vector from $\boldsymbol{x}'$ to $\boldsymbol{x}$ and using the spherical Bessel function j_ℓ and the spherical harmonics $Y_{\ell m}$, we can write

$$\mathrm{e}^{i\boldsymbol{k}\cdot\boldsymbol{R}} = 4\pi \sum_{\ell=0}^{\infty} \sum_{m=-\ell}^{\ell} i^\ell Y_{\ell m}^*(\theta_k, \phi_k) j_\ell(kR) Y_{\ell m}(\theta_R, \phi_R) \,, \tag{4.10}$$

where $R := |\boldsymbol{R}|$, and ℓ and m are degree and order of the spherical harmonics, respectively. We remark that θ_R and ϕ_R are angles between $\boldsymbol{x}'$ and $\boldsymbol{R}$. Now, the model-dependent part in the ORF (4.6) can also be expanded by the spherical harmonics as

$$f^{(\lambda)}(\mu_k) N^{(\lambda)} = \sum_{\ell'=0}^{\infty} a_{\ell'0}^{(\lambda)} Y_{\ell'0}(\theta_k) \,, \tag{4.11}$$

---

[9]In ref. [60], the angular integral is directly integrated using the Bessel function, where the method is explained in appendix B.

where $a_{\ell'0}^{(\lambda)}$ denote model-dependent coefficients. We have imposed a condition that the order is zero because the coordinate system have been chosen so that the azimuthal angle ϕ_k is zero (see eq. (4.9)). It is now clear that the angular integral can be performed using the property of the spherical harmonics

$$\int \mathrm{d}\Omega_k Y_{\ell m}^*(\theta_k, \phi_k) Y_{\ell' m'}(\theta_k, \phi_k) = \delta_{\ell \ell'} \delta_{mm'} . \tag{4.12}$$

We finally note that the ORF is a function of the distances and the angle from an observer, while, after using the property (4.12), we are left with the separation between two galaxies R and the angle between the LOS and the separation vector θ_R. Defining

$$\Delta r := r' - r = \eta - \eta' , \tag{4.13}$$

which is bounded as $\Delta r > -r$, the separation distance R can be rewritten as

$$R = \sqrt{r^2 + (r')^2 - 2rr' \cos\theta} = r\sqrt{1 + \left(1 + \frac{k\Delta r}{kr}\right)^2 - 2\left(1 + \frac{k\Delta r}{kr}\right)\cos\theta} , \tag{4.14}$$

and the angles are related as

$$\theta_R = \theta + \arccos \frac{1 - \left(1 + \frac{k\Delta r}{kr}\right)\cos\theta}{\sqrt{1 + \left(1 + \frac{k\Delta r}{kr}\right)^2 - 2\left(1 + \frac{k\Delta r}{kr}\right)\cos\theta}} . \tag{4.15}$$

4.2   Computing the ORF: examples

As representative examples, let us investigate the ORFs of the projected tensor and vector fields in the presence of the helicity-one and helicity-zero modes. We assume that the longitudinal mode corresponding to the gravitational potential is constant in time and the helicity-two modes propagate at the speed of light. These assumptions would be reasonable considering current cosmological observations and the GW170817 event [73].

4.2.1   Auto correlation of the traceless tensor field

Let us first consider the auto correlation of the traceless tensor field. The function $\hat{\Gamma}$, defined in eq. (4.7), is a function of the directional cosine μ_k and we can write it in terms of the spherical harmonics as

$$\hat{\Gamma}_{h^{\mathrm{T}} h^{\mathrm{T}}} = \sum_{i=0,2,4} C_i^{h^{\mathrm{T}} h^{\mathrm{T}}} Y_{i0}(\theta_k) , \tag{4.16}$$

where coefficients $C_i^{h^{\mathrm{T}} h^{\mathrm{T}}}$ are explicitly given by

$$C_0^{h^{\mathrm{T}} h^{\mathrm{T}}} = \frac{4\sqrt{\pi}}{15} \left[3N^{(\mathrm{T})} \cos(k\Delta r) + 3N^{(\mathrm{V})} \cos(c_{\mathrm{v}} k\Delta r) + N^{(b)} \cos(c_{\mathrm{s}} k\Delta r) \right] , \tag{4.17}$$

$$C_2^{h^{\mathrm{T}} h^{\mathrm{T}}} = \frac{4}{21}\sqrt{\frac{\pi}{5}} \left[6N^{(\mathrm{T})} \cos(k\Delta r) - 3N^{(\mathrm{V})} \cos(c_{\mathrm{v}} k\Delta r) - 2N^{(b)} \cos(c_{\mathrm{s}} k\Delta r) \right] , \tag{4.18}$$

$$C_4^{h^{\mathrm{T}} h^{\mathrm{T}}} = \frac{2\sqrt{\pi}}{105} \left[N^{(\mathrm{T})} \cos(k\Delta r) - 4N^{(\mathrm{V})} \cos(c_{\mathrm{v}} k\Delta r) + 2N^{(b)} \cos(c_{\mathrm{s}} k\Delta r) \right] , \tag{4.19}$$
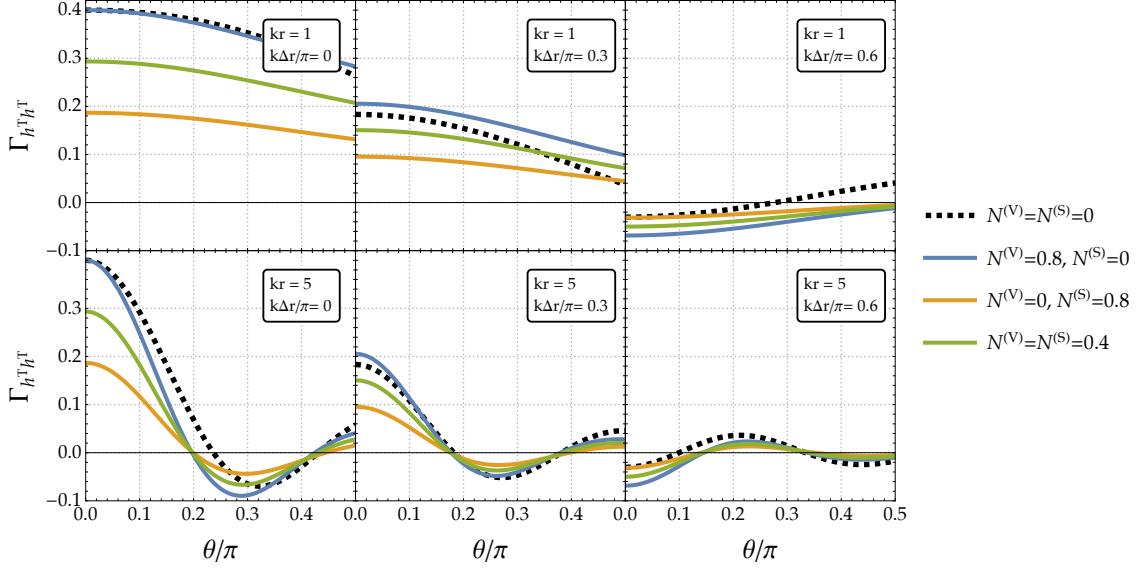
Figure 1: Auto correlations of the projected traceless tensor field with $c_\lambda = 1$. The black dashed line corresponds to the standard transverse and traceless GWs. The blue (orange) line is depicted if the vector (scalar) power spectrum has 80% of the total power. The green line is the case where 80% of the total power is equally distributed to the scalar and vector parts.

with

$$N^{(\mathrm{T})} := N^{(+2)} + N^{(-2)} , \quad N^{(\mathrm{V})} := N^{(+1)} + N^{(-1)} . \tag{4.20}$$

Recalling the property of the spherical harmonics (4.12), it is immediate to see that the ORF takes the form

$$\Gamma_{h^\mathrm{T} h^\mathrm{T}} = \sum_{\ell=0,2,4} i^\ell C_\ell^{h^\mathrm{T} h^\mathrm{T}} Y_{\ell 0}(\theta_k) j_\ell(kR) . \tag{4.21}$$

Figure 1 shows the ORF of the projected traceless tensor (4.21) with sound speed $c_\lambda = 1$. The black line corresponds to the case where only the helicity-two modes are taken into account, thereby being a fiducial line. As can be seen, the presence of additional modes can change the amplitude and the shape of the ORF. Thus, in principle, an accurate data of galaxy redshift survey enables us to verify whether or not the GWs carry extra polarizations on top of the helicity-two modes. When performing template matching, however, we need to pay attention to the possibility where the sound speed of the vector and scalar modes can be different from the speed of light. Since the sound speed appears in the oscillation term as $\cos{(c_\lambda k \Delta r)}$, the effect becomes large unless $(1 - c_\lambda)k\Delta r \pmod{2\pi} \ll 1$. Figure 2 shows the dependence of the sound speed c_λ on the ORF. We see that the ORFs are indeed identical in the limit of $k\Delta r = 0$, and they can be different for other parameters. This property implies that we can estimate the amount of contamination from the vector and scalar modes without being affected by their unknown sound speed if we observe galaxies at the same distance from us.

4.2.2 Vector cross correlation

Let us next investigate the ORF of the vector cross correlation which is a suitable correlation to see signals of parity violation. As can be seen eq. (3.19), the function $\hat{\Gamma}$ in this case is an odd polynomial of μ_k, so that
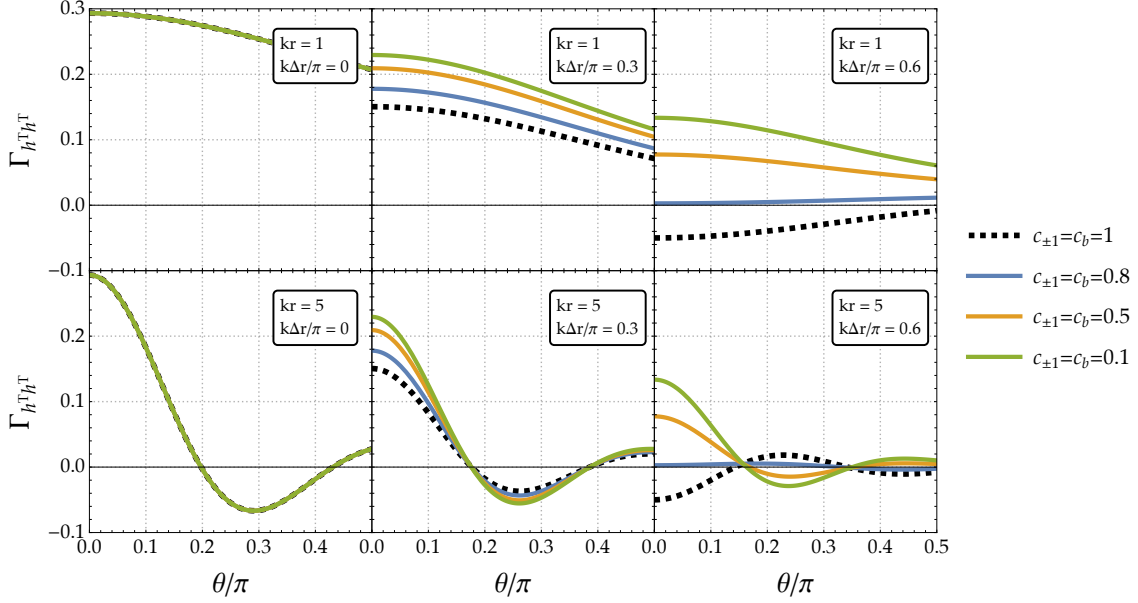
Figure 2: Auto correlations of the projected traceless tensor field with different vector's sound speeds. The black dashed line is the fiducial line corresponding to the standard transverse and traceless GWs. The distribution of the power is fixed to be $N^{(\mathrm{T})} = 0.2$, $N^{(\mathrm{V})} = N^{(\mathrm{S})} = 0.4$, which corresponds to the green line in figure 1.

it can be expanded by the spherical harmonics with odd degree

$$\hat{\Gamma}_{\widetilde{V}^{\mathrm{T}}V^{\mathrm{T}}} = \sum_{i=1,3,5} C_i^{\widetilde{V}^{\mathrm{T}}V^{\mathrm{T}}} Y_{i0}(\theta_k) \,, \tag{4.22}$$

where the coefficients $C_i^{\widetilde{V}^{\mathrm{T}}V^{\mathrm{T}}}$ are explicitly given by

$$C_1^{\widetilde{V}^{\mathrm{T}}V^{\mathrm{T}}} = i\frac{2}{35}\sqrt{\frac{\pi}{3}}\left[-5\widetilde{N}^{(\mathrm{T})}\cos\left(k\Delta r\right) - 4\widetilde{N}^{(\mathrm{V})}\cos\left(c_{\mathrm{v}}k\Delta r\right)\right] \,, \tag{4.23}$$

$$C_3^{\widetilde{V}^{\mathrm{T}}V^{\mathrm{T}}} = i\frac{2}{45}\sqrt{\frac{\pi}{7}}\left[5\widetilde{N}^{(\mathrm{T})}\cos\left(k\Delta r\right) + 8\widetilde{N}^{(\mathrm{V})}\cos\left(c_{\mathrm{v}}k\Delta r\right)\right] \,, \tag{4.24}$$

$$C_5^{\widetilde{V}^{\mathrm{T}}V^{\mathrm{T}}} = i\frac{4}{63}\sqrt{\frac{\pi}{11}}\left[\widetilde{N}^{(\mathrm{T})}\cos\left(k\Delta r\right) - 2\widetilde{N}^{(\mathrm{V})}\cos\left(c_{\mathrm{v}}k\Delta r\right)\right] \,. \tag{4.25}$$

Here, we introduce

$$\widetilde{N}^{(\mathrm{T})} := N^{(+2)} - N^{(-2)} \,, \quad \widetilde{N}^{(\mathrm{V})} := N^{(+1)} - N^{(-1)} \,. \tag{4.26}$$

Being similar to the previous subsection, the ORF is expressed as

$$\Gamma_{\widetilde{V}^{\mathrm{T}}V^{\mathrm{T}}} = \sum_{\ell=1,3,5} i^\ell C_\ell^{\widetilde{V}^{\mathrm{T}}V^{\mathrm{T}}} Y_{\ell 0}(\theta_k) j_\ell(kR) \,. \tag{4.27}$$

Figure 3 shows the ORF of the vector cross-correlation assuming, for simplicity, a maximal chirality for the helicity-two and helicity-one modes, namely, $\chi^{(\mathrm{T})} = \chi^{(\mathrm{V})} = 1$. We also assume that the helicity-one
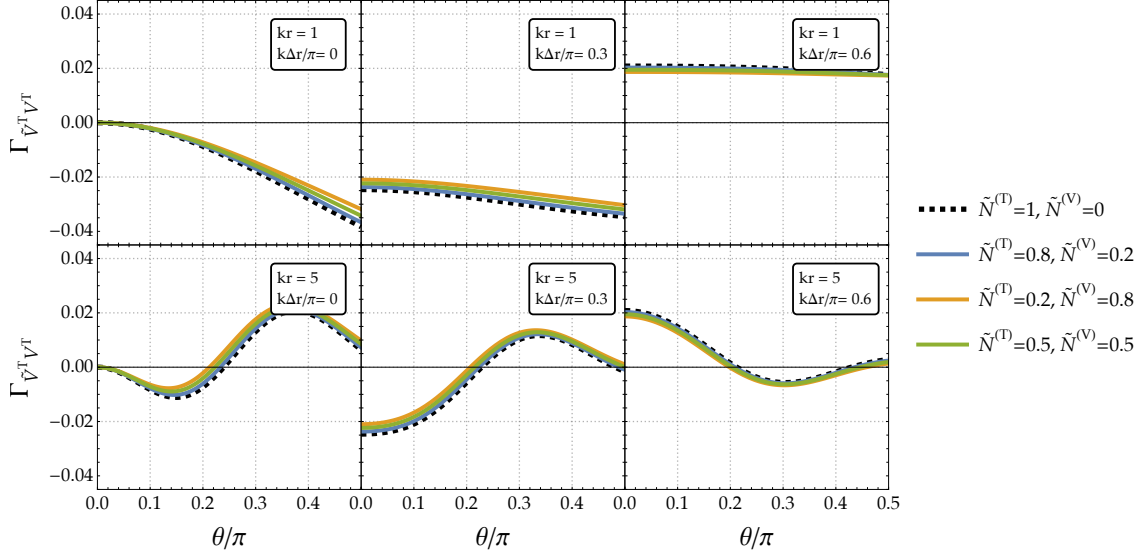
Figure 3: Cross correlation of the vector and curl vector assuming that the helicity-two and helicity-one modes are maximally chiral and $c_{+1} = 1$. The black dashed line is depicted without the vector mode. We set the speed of the helicity-one wave equals to the speed of light.

wave propagates at the speed of light. The black dashed line shows the ORF in the case when only the left-handed helicity-two wave is present while other lines contain some amount of the left-handed vector wave. The amplitude depends on the amount of the helicity-one mode but overall shape of the ORF remains almost unchanged. Figure 4 shows the dependence of the sound speed of the helicity-one wave on the vector cross-correlation. We can see that, if the helicity-one mode propagates slower than light, the ORF exhibits different behaviors unless $(1 - c_{+1})k\Delta r \pmod{2\pi} \ll 1$. Thus, if parity violation exists and the sound speeds of the modes differ, upcoming observations of the large-scale structure may provide insights into the underlying physics of the primordial universe.

5 Conclusions

We have studied the three-dimensional correlation functions using the tensor field projected onto the two-dimensional space and investigated how extra polarization modes beyond GR can change the spectra. In particular, we have focused on the traceless components of the projected tensor field to isolate intrinsic contributions of galaxies. We have found that the amplitude and angular dependence of the analogue of the ORF used in PTA observations can vary depending on the presence of the extra polarizations, differences in their propagation speeds, and the LOS distances to galaxies (see figure 1 and figure 2). We have also studied the vector cross correlation that can find out parity-violating signals when restricting operators constructed by the traceless projected tensor. When the extra vector mode propagates at the speed of light, the shape of the ORF is nearly the same irrespective of the amount of the power of the vector mode, while its amplitude is slightly changed. If the vector mode propagates slower than the tensor mode, i.e., the speed of light, the ORF can exhibit a different behavior (see figure 3 and figure 4).

The IAs contain valuable information about underlying physics of the universe and, since GWs may leave imprints on shapes of galaxies through the tidal effect, it is possible to probe the nature of GWs at frequencies that have not been investigated well. This work have generalized ref. [60] to some extent in preparation for
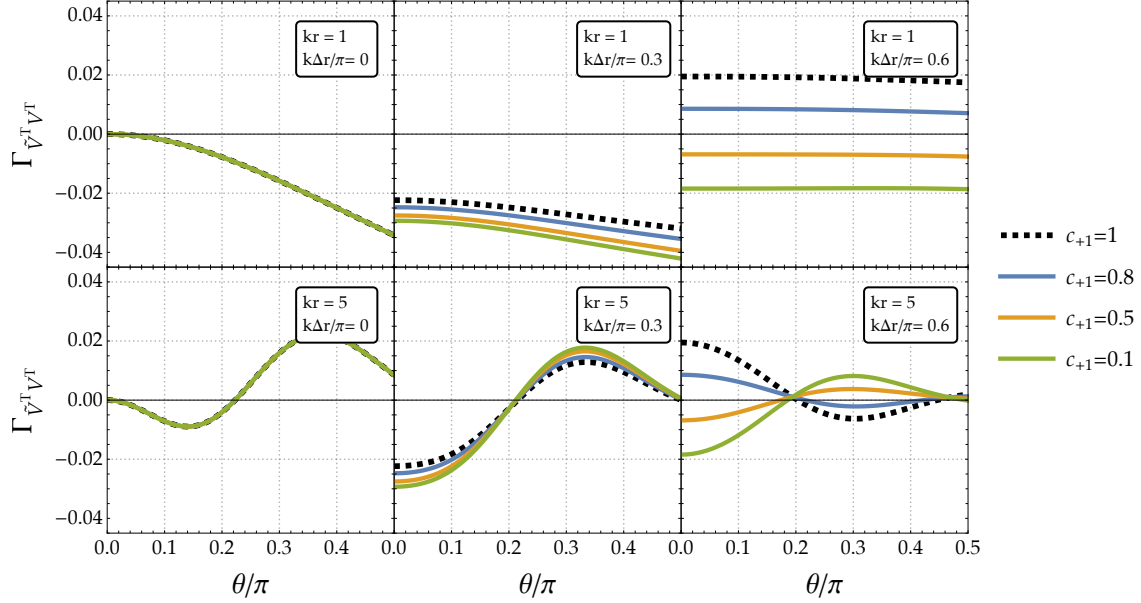
Figure 4: Dependence of the speed of the helicity-one wave on the cross correlation of the vector and curl vector assuming a maximal chirality for the helicity-two and helicity-one modes. The distribution of the power is fixed to be $\widetilde{N}^{(+2)} = \widetilde{N}^{(+1)} = 0.5$, which corresponds to the green line in figure 3.

fitting modified theories of gravity with a wealth of galaxy survey data. However, we still lack theoretical foundations because we have restricted ourselves to a limited class of models with the dispersion relation $\omega_\lambda = c_\lambda k$. The form of the dispersion is modified if we consider, for instance, massive gravity or massive scalar-tensor theories. In such cases, propagation speed depends on frequency, so that the ORF is subjected to change. Besides, we adopt the flat-sky approximation in this work to simplify the discussion. Thus this work should be further generalized to derive full-sky expressions. We leave these studies for future research.

Acknowledgments

A   Power spectra of the projected tensor field without extracting trace

In section 3, we have focused on the traceless part of the projected tensor field in light of the observational difficulty in studying its trace component. Here, we list the power spectra of the projected tensor field without extracting its trace.

A.1 Projected tensor field

The power spectrum of the projected tensor field is given by

$$\left\langle h^{AB}(\eta, \boldsymbol{k}) h_{AB}(\eta', \boldsymbol{k}') \right\rangle = (2\pi)^3 \, \delta_D^{(2)}(\boldsymbol{k} + \boldsymbol{k}') F_{hh}(\mu_k, \eta, \eta', k) \, , \tag{A.1}$$

with

$$F_{hh}(\mu_k, \eta, \eta', k) = \frac{1}{4} \left(1 + \mu_k^2\right)^2 P^{(\mathrm{T})}(\eta, \eta', k) + \frac{1}{2} \left(1 + \mu_k^2 - 2\mu_k^4\right) P^{(\mathrm{V})}(\eta, \eta', k)$$
$$+ \frac{1}{2} \left(1 + \mu_k^4\right) P^{(b)}(\eta, \eta', k) + \left(1 - \mu_k^2\right)^2 P^{(\ell)}(\eta, \eta', k) \, . \tag{A.2}$$

A.2 Projected vector field

As in section 3.3, one can define two different vectors out of the projected tensor field as

$$h_A(\eta, \boldsymbol{k}) := i k^B h_{BA}(\eta, \boldsymbol{k}) \, , \tag{A.3}$$

$$\widetilde{h}_A(\eta, \boldsymbol{k}) := i \epsilon^{BC} k_B h_{CA}(\eta, \boldsymbol{k}) \, . \tag{A.4}$$

Their auto power spectra are defined by

$$\left\langle h^A(\eta, \boldsymbol{k}) h_A(\eta', \boldsymbol{k}') \right\rangle = (2\pi)^3 \, \delta_D^{(2)}(\boldsymbol{k} + \boldsymbol{k}') F_{VV}(\mu_k, \eta, \eta', k) \, , \tag{A.5}$$

$$\left\langle \widetilde{h}^A(\eta, \boldsymbol{k}) \widetilde{h}_A(\eta', \boldsymbol{k}') \right\rangle = (2\pi)^3 \, \delta_D^{(2)}(\boldsymbol{k} + \boldsymbol{k}') F_{\widetilde{V}\widetilde{V}}(\mu_k, \eta, \eta', k) \, , \tag{A.6}$$

where the functions F_{VV} and $F_{\widetilde{V}\widetilde{V}}$ are respectively given by

$$F_{VV}(\mu_k, \eta, \eta', k) = \frac{1}{4} k^2 \mu_k^2 \left(1 - \mu_k^4\right) P^{(\mathrm{T})}(\eta, \eta', k) + \frac{1}{4} k^2 \left(1 - \mu_k^2\right)^2 \left(1 + 4\mu_k^2\right) P^{(\mathrm{V})}(\eta, \eta', k)$$
$$+ \frac{1}{2} k^2 \mu_k^4 \left(1 - \mu_k^2\right) P^{(b)}(\eta, \eta', k) + k^2 \left(1 - \mu_k^2\right)^3 P^{(\ell)}(\eta, \eta', k) \, , \tag{A.7}$$

and

$$F_{\widetilde{V}\widetilde{V}}(\mu_k, \eta, \eta', k) = \frac{1}{4} k^2 \left(1 - \mu_k^4\right) P^{(\mathrm{T})}(\eta, \eta', k) + \frac{1}{4} k^2 \left(1 - \mu_k^2\right)^2 P^{(\mathrm{V})}(\eta, \eta', k)$$
$$+ \frac{1}{2} k^2 \left(1 - \mu_k^2\right) P^{(b)}(\eta, \eta', k) \, . \tag{A.8}$$

We notice that there is no longitudinal contribution in the auto power spectrum of the curl vector $\widetilde{h}_A$. The cross correlation of the two different vectors becomes nonzero with chiral GWs as

$$\left\langle \widetilde{h}^A(\eta, \boldsymbol{k}) h_A(\eta', \boldsymbol{k}') \right\rangle = (2\pi)^3 \, \delta_D^{(2)}(\boldsymbol{k} + \boldsymbol{k}') F_{\widetilde{V}V}(\mu_k, \eta, \eta', k) \, , \tag{A.9}$$

where the kernel function is

$$F_{\widetilde{V}V}(\mu_k, \eta, \eta', k) = -\frac{i}{4} k^2 \mu_k \left(1 - \mu_k^4\right) \chi^{(\mathrm{T})} P^{(\mathrm{T})}(\eta, \eta', k) - \frac{i}{2} k^2 \mu_k \left(1 - \mu_k^2\right)^2 \chi^{(\mathrm{V})} P^{(\mathrm{V})}(\eta, \eta', k) \, . \tag{A.10}$$

15

A.3 Projected scalar field

Let us move on to scalar quantities. Due to the presence of the trace of the projected tensor field, one can introduce three different types of scalar fields as

$$\psi(\eta, \mathbf{k}) := g^{AB} h_{AB}(\eta, \mathbf{k}) , \quad S(\eta, \mathbf{k}) := ik^A h_A(\eta, \mathbf{k}) , \quad \widetilde{S}(\eta, \mathbf{k}) := ik^A \widetilde{h}_A(\eta, \mathbf{k}) . \tag{A.11}$$

The first one is a trace component of the projected tensor field, whose power spectrum is defined by

$$\langle \psi(\eta, \mathbf{k}) \psi(\eta', \mathbf{k}') \rangle = (2\pi)^3 \delta_D^{(2)}(\mathbf{k} + \mathbf{k}') F_{\psi\psi}(\mu_k, \eta, \eta', k) , \tag{A.12}$$

with

$$F_{\psi\psi}(\mu_k, \eta, \eta', k) = \frac{1}{4} \left(1 - \mu_k^2\right)^2 P^{(\mathrm{T})}(\eta, \eta', k) + \mu_k^2 \left(1 - \mu_k^2\right) P^{(\mathrm{V})}(\eta, \eta', k)$$
$$+ \frac{1}{2} \left(1 + \mu_k^2\right)^2 P^{(b)}(\eta, \eta', k) + \left(1 - \mu_k^2\right)^2 P^{(\ell)}(\eta, \eta', k) . \tag{A.13}$$

The other auto power spectra are defined respectively as

$$\langle S(\eta, \mathbf{k}) S(\eta', \mathbf{k}') \rangle = (2\pi)^3 \delta_D^{(2)}(\mathbf{k} + \mathbf{k}') F_{SS}(\mu_k, \eta, \eta', k) , \tag{A.14}$$

with

$$F_{SS}(\mu_k, \eta, \eta', k) = \frac{1}{4} k^4 \mu_k^4 \left(1 - \mu_k^2\right)^2 P^{(\mathrm{T})}(\eta, \eta', k) + k^4 \mu_k^2 \left(1 - \mu_k^2\right)^3 P^{(\mathrm{V})}(\eta, \eta', k)$$
$$+ \frac{1}{2} k^4 \mu_k^4 \left(1 - \mu_k^2\right)^2 P^{(b)}(\eta, \eta', k) + k^4 \left(1 - \mu_k^2\right)^4 P^{(\ell)}(\eta, \eta', k) , \tag{A.15}$$

and

$$\left\langle \widetilde{S}(\eta, \mathbf{k}) \widetilde{S}(\eta', \mathbf{k}') \right\rangle = (2\pi)^3 \delta_D^{(2)}(\mathbf{k} + \mathbf{k}') F_{\widetilde{S}\widetilde{S}}(\mu_k, \eta, \eta', k) , \tag{A.16}$$

with

$$F_{\widetilde{S}\widetilde{S}}(\mu_k, \eta, \eta', k) = \frac{1}{4} k^4 \mu_k^2 \left(1 - \mu_k^2\right)^2 P^{(\mathrm{T})}(\eta, \eta', k) + \frac{1}{4} k^4 \left(1 - \mu_k^2\right)^3 P^{(\mathrm{V})}(\eta, \eta', k) . \tag{A.17}$$

There can be three types of cross correlations. The cross correlations with the trace are given by

$$\langle \psi(\eta, \mathbf{k}) S(\eta', \mathbf{k}') \rangle = (2\pi)^3 \delta_D^{(2)}(\mathbf{k} + \mathbf{k}') F_{\psi S}(\mu_k, \eta, \eta', k) , \tag{A.18}$$

$$\left\langle \psi(\eta, \mathbf{k}) \widetilde{S}(\eta', \mathbf{k}') \right\rangle = (2\pi)^3 \delta_D^{(2)}(\mathbf{k} + \mathbf{k}') F_{\psi\widetilde{S}}(\mu_k, \eta, \eta', k) , \tag{A.19}$$

where their kernel functions are

$$F_{\psi S}(\mu_k, \eta, \eta', k) = \frac{1}{4} k^2 \mu_k^2 \left(1 - \mu_k^2\right)^2 P^{(\mathrm{T})}(\eta, \eta', k) - \frac{1}{2} k^2 \mu_k^2 \left(1 - \mu_k^2\right)^2 P^{(\mathrm{V})}(\eta, \eta', k)$$
$$- \frac{1}{2} k^2 \mu_k^2 \left(1 - \mu_k^4\right) P^{(b)}(\eta, \eta', k) - k^2 \left(1 - \mu_k^2\right)^3 P^{(\ell)}(\eta, \eta', k) , \tag{A.20}$$

and

$$F_{\psi\widetilde{S}}(\mu_k, \eta, \eta', k) = \frac{i}{4} k^2 \mu_k \left(1 - \mu_k^2\right)^2 \chi^{(\mathrm{T})} P^{(\mathrm{T})}(\eta, \eta', k) - \frac{i}{2} k^2 \mu_k \left(1 - \mu_k^2\right)^2 \chi^{(\mathrm{V})} P^{(\mathrm{V})}(\eta, \eta', k) . \tag{A.21}$$

The remaining cross-correlation is

$$\left\langle \widetilde{S}(\eta, \mathbf{k}) S(\eta', \mathbf{k}') \right\rangle = (2\pi)^3 \delta_D^{(2)}(\mathbf{k} + \mathbf{k}') F_{\widetilde{S}S}(\mu_k, \eta, \eta', k) , \tag{A.22}$$

with

$$F_{\widetilde{S}S}(\mu_k, \eta, \eta', k) = -\frac{i}{4} k^4 \mu_k^3 \left(1 - \mu_k^2\right)^2 \chi^{(\mathrm{T})} P^{(\mathrm{T})}(\eta, \eta', k) - \frac{i}{2} k^4 \mu_k \left(1 - \mu_k^2\right)^3 \chi^{(\mathrm{V})} P^{(\mathrm{V})}(\eta, \eta', k) . \tag{A.23}$$

16

B A different way of calculating the angular integral

While we used the spherical harmonics to perform the angular integral of the ORF in section 4, it can be analyzed directly as done in ref. [60]. Here, with one example, we show that these two ways of calculation give the same result.

Let us consider the following two-point function

$$\Gamma_{h^{\mathrm{T}} h^{\mathrm{T}}} = \cos\left(k\Delta r\right) \int d\Omega_k \frac{1}{8} \left(1 + 6\mu_k^2 + \mu_k^4\right) e^{i\boldsymbol{k}\cdot(\boldsymbol{x}-\boldsymbol{x}')} . \tag{B.1}$$

With the coordinate system

$$x'^{\mu} = \left(\eta', 0, 0, r'\right) , \quad x^{\mu} = \left(\eta, r\sin\theta\cos\theta, r\sin\theta\sin\theta, r\cos\theta\right) , \tag{B.2}$$

and the wavevector

$$\boldsymbol{k} = \left(k\sin\theta_k\cos\theta_k, k\sin\theta_k\sin\theta_k, k\cos\theta_k\right) , \tag{B.3}$$

the exponential function reduces to

$$e^{i\boldsymbol{k}\cdot(\boldsymbol{x}-\boldsymbol{x}')} = \exp\left[ikr\mu_k\left\{\cos\theta - \left(1 + \frac{k\Delta r}{kr}\right)\right\}\right] e^{ikr\sqrt{1-\mu_k^2}\cos(\phi-\phi_k)\sin\theta} . \tag{B.4}$$

The ϕ_k-integral can be performed analytically as

$$\int_0^{2\pi} d\phi_k e^{i\boldsymbol{k}\cdot(\boldsymbol{x}-\boldsymbol{x}')} = 2\pi \exp\left[ikr\mu_k\left\{\cos\theta - \left(1 + \frac{k\Delta r}{kr}\right)\right\}\right] J_0\left(kr\sqrt{1-\mu_k^2}\sin\theta\right) , \tag{B.5}$$

where J_0 is the zeroth order Bessel function of first kind. We eventually find that the ORF takes the form

$$\Gamma_{h^{\mathrm{T}} h^{\mathrm{T}}} = \cos\left(k\Delta r\right) \int_1^1 d\mu_k \frac{1 + 6\mu_k^2 + \mu_k^4}{16} e^{-i\mu_k\{k\Delta r + 2kr\sin^2(\theta/2)\}} J_0\left(kr\sqrt{1-\mu_k^2}\sin\theta\right) . \tag{B.6}$$

Figure 5 shows the above ORF with different parameters, implying that the two ways of calculations agree each other.
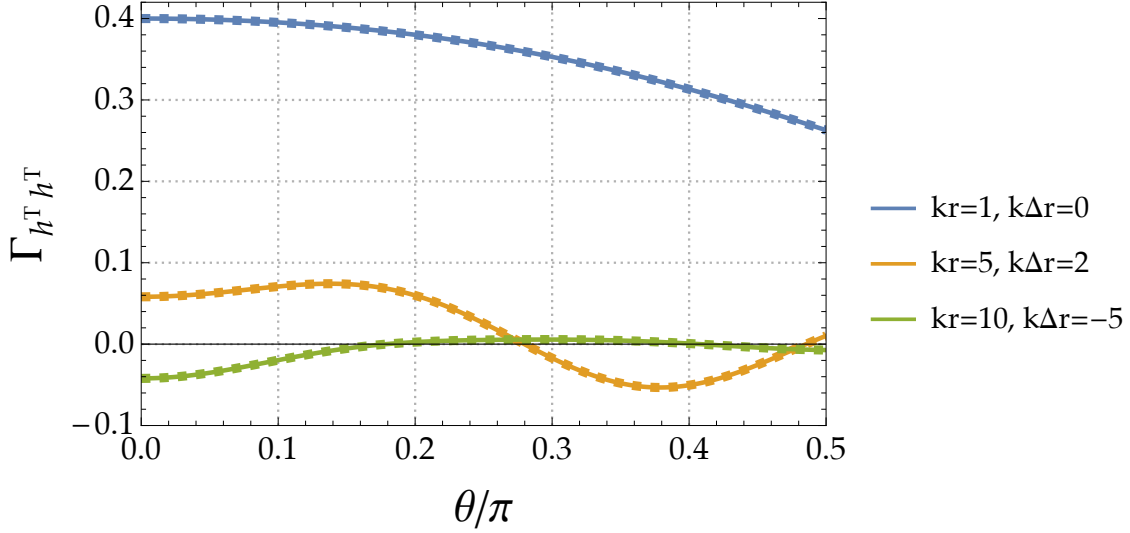
Figure 5: The overlap reduction function obtained from the direct integration of eq. (B.6) (solid line) and the spherical harmonics expansion (4.21) with $s = v = 0$ (dashed line). With several parameters, we check that the two ways give the same results.

References

[1] LIGO SCIENTIFIC, VIRGO collaboration, *Observation of Gravitational Waves from a Binary Black Hole Merger*, *Phys. Rev. Lett.* **116** (2016) 061102 [1602.03837].

[2] LIGO SCIENTIFIC, VIRGO collaboration, *Tests of general relativity with GW150914*, *Phys. Rev. Lett.* **116** (2016) 221101 [1602.03841].

[3] LIGO SCIENTIFIC, VIRGO collaboration, *GW151226: Observation of Gravitational Waves from a 22-Solar-Mass Binary Black Hole Coalescence*, *Phys. Rev. Lett.* **116** (2016) 241103 [1606.04855].

[4] LIGO SCIENTIFIC, VIRGO collaboration, *Binary Black Hole Mergers in the first Advanced LIGO Observing Run*, *Phys. Rev. X* **6** (2016) 041015 [1606.04856].

[5] N. Yunes, K. Yagi and F. Pretorius, *Theoretical Physics Implications of the Binary Black-Hole Mergers GW150914 and GW151226*, *Phys. Rev. D* **94** (2016) 084002 [1603.08955].

[6] KAGRA, LIGO SCIENTIFIC, VIRGO collaboration, *Prospects for observing and localizing gravitational-wave transients with Advanced LIGO, Advanced Virgo and KAGRA*, *Living Rev. Rel.* **19** (2016) 1 [1304.0670].

[7] VIRGO collaboration, *Advanced Virgo: a second-generation interferometric gravitational wave detector*, *Class. Quant. Grav.* **32** (2015) 024001 [1408.3978].

[8] LIGO SCIENTIFIC collaboration, *Advanced LIGO*, *Class. Quant. Grav.* **32** (2015) 074001 [1411.4547].

[9] TIANQIN collaboration, *TianQin: a space-borne gravitational wave detector*, *Class. Quant. Grav.* **33** (2016) 035010 [1512.02076].

[10] LISA collaboration, *Laser Interferometer Space Antenna*, 1702.00786.

[11] S. Kawamura et al., *Current status of space gravitational wave antenna DECIGO and B-DECIGO*, *PTEP* **2021** (2021) 05A105 [2006.13545].

[12] NANOGRAV collaboration, *The NANOGrav 12.5 yr Data Set: Search for an Isotropic Stochastic Gravitational-wave Background*, *Astrophys. J. Lett.* **905** (2020) L34 [2009.04496].

[13] J. Lee and U.-L. Pen, *Cosmic shear from galaxy spins*, *Astrophys. J. Lett.* **532** (2000) L5 [astro-ph/9911328].

[14] P. Catelan, M. Kamionkowski and R.D. Blandford, *Intrinsic and extrinsic galaxy alignment*, *Mon. Not. Roy. Astron. Soc.* **320** (2001) L7 [astro-ph/0005470].

[15] R.G. Crittenden, P. Natarajan, U.-L. Pen and T. Theuns, *Spin induced galaxy alignments and their implications for weak lensing measurements*, *Astrophys. J.* **559** (2001) 552 [astro-ph/0009052].

[16] C.M. Hirata and U. Seljak, *Intrinsic alignment-lensing interference as a contaminant of cosmic shear*, *Phys. Rev. D* **70** (2004) 063526 [astro-ph/0406275].

[17] M.A. Troxel and M. Ishak, *The Intrinsic Alignment of Galaxies and its Impact on Weak Gravitational Lensing in an Era of Precision Cosmology*, *Phys. Rept.* **558** (2014) 1 [1407.6990].

[18] B. Joachimi et al., *Galaxy alignments: An overview*, *Space Sci. Rev.* **193** (2015) 1 [1504.05456].

[19] J. Blazek, M. McQuinn and U. Seljak, *Testing the tidal alignment model of galaxy intrinsic alignment*, *JCAP* **05** (2011) 010 [1101.4017].

[20] T. Okumura, A. Taruya and T. Nishimichi, *Intrinsic alignment statistics of density and velocity fields at large scales: Formulation, modeling and baryon acoustic oscillation features*, *Phys. Rev. D* **100** (2019) 103507 [1907.00750].

[21] T. Okumura, Y.P. Jing and C. Li, *Intrinsic Ellipticity Correlation of SDSS Luminous Red Galaxies and Misalignment with their Host Dark Matter Halos*, *Astrophys. J.* **694** (2009) 214 [0809.3790].

[22] T. Okumura and Y.P. Jing, *The Gravitational Shear – Intrinsic Ellipticity Correlation Functions of Luminous Red Galaxies in Observation and in ΛCDM model*, *Astrophys. J. Lett.* **694** (2009) L83 [0812.2935].

[23] N.E. Chisari and C. Dvorkin, *Cosmological Information in the Intrinsic Alignments of Luminous Red Galaxies*, *JCAP* **12** (2013) 029 [1308.5972].

[24] F. Schmidt, N.E. Chisari and C. Dvorkin, *Imprint of inflation on galaxy shape correlations*, *JCAP* **10** (2015) 032 [1506.02671].

[25] N.E. Chisari, C. Dvorkin, F. Schmidt and D. Spergel, *Multitracing Anisotropic Non-Gaussianity with Galaxy Shapes*, *Phys. Rev. D* **94** (2016) 123507 [1607.05232].

[26] K. Kogai, K. Akitsu, F. Schmidt and Y. Urakawa, *Galaxy imaging surveys as spin-sensitive detector for cosmological colliders*, *JCAP* **03** (2021) 060 [2009.05517].

[27] J. Lee, S. Ryu and M. Baldi, *Disentangling Modified Gravity and Massive Neutrinos with Intrinsic Shape Alignments of Massive Halos*, *Astrophys. J.* **945** (2023) 15 [2206.03406].

[28] T. Okumura and A. Taruya, *Anisotropies of galaxy ellipticity correlations in real and redshift space: angular dependence in linear tidal alignment model*, *Mon. Not. Roy. Astron. Soc.* **493** (2020) L124 [1912.04118].

[29] T. Okumura, A. Taruya and T. Nishimichi, *Testing tidal alignment models for anisotropic correlations of halo ellipticities with N-body simulations*, *Mon. Not. Roy. Astron. Soc.* **494** (2020) 694 [2001.05302].

[30] K. Akitsu, T. Kurita, T. Nishimichi, M. Takada and S. Tanaka, *Imprint of anisotropic primordial non-Gaussianity on halo intrinsic alignments in simulations*, *Phys. Rev. D* **103** (2021) 083508 [2007.03670].

[31] K. Akitsu, Y. Li and T. Okumura, *Cosmological simulation in tides: power spectra, halo shape responses, and shape assembly bias*, *JCAP* **04** (2021) 041 [`2011.06584`].

[32] M. Shiraishi, A. Taruya, T. Okumura and K. Akitsu, *Wide-angle effects on galaxy ellipticity correlations*, *Mon. Not. Roy. Astron. Soc.* **503** (2021) L6 [`2012.13290`].

[33] J. Shi, K. Osato, T. Kurita and M. Takada, *An Optimal Estimator of Intrinsic Alignments for Star-forming Galaxies in IllustrisTNG Simulation*, *Astrophys. J.* **917** (2021) 109 [`2104.12329`].

[34] T. Kurita and M. Takada, *Analysis method for 3D power spectrum of projected tensor fields with fast estimator and window convolution modeling: An application to intrinsic alignments*, *Phys. Rev. D* **105** (2022) 123501 [`2202.11839`].

[35] A. Taruya and T. Okumura, *Improving geometric and dynamical constraints on cosmology with intrinsic alignments of galaxies*, *Astrophys. J. Lett.* **891** (2020) 043523 [`2001.05962`].

[36] T. Kurita, M. Takada, T. Nishimichi, R. Takahashi, K. Osato and Y. Kobayashi, *Power spectrum of halo intrinsic alignments in simulations*, *Mon. Not. Roy. Astron. Soc.* **501** (2021) 833 [`2004.12579`].

[37] T. Okumura and A. Taruya, *Tightening geometric and dynamical constraints on dark energy and gravity: Galaxy clustering, intrinsic alignment, and kinetic Sunyaev-Zel'dovich effect*, *Phys. Rev. D* **106** (2022) 043523 [`2110.11127`].

[38] Y.-T. Chuang, T. Okumura and M. Shirasaki, *Distinguishing between ΛCDM and f(R) gravity models using halo ellipticity correlations in simulations*, *Mon. Not. Roy. Astron. Soc.* **515** (2022) 4464 [`2111.01417`].

[39] S. Saga, T. Okumura, A. Taruya and T. Inoue, *Relativistic distortions in galaxy density–ellipticity correlations: gravitational redshift and peculiar velocity effects*, *Mon. Not. Roy. Astron. Soc.* **518** (2023) 4976 [`2207.03454`].

[40] M. Shiraishi, T. Okumura and K. Akitsu, *Statistical anisotropy in galaxy ellipticity correlations*, *JCAP* **08** (2023) 013 [`2303.10890`].

[41] T. Okumura and A. Taruya, *First Constraints on Growth Rate from Redshift-space Ellipticity Correlations of SDSS Galaxies at 0.16 < z < 0.70*, *Astrophys. J. Lett.* **945** (2023) L30 [`2301.06273`].

[42] T. Kurita and M. Takada, *Constraints on anisotropic primordial non-Gaussianity from intrinsic alignments of SDSS-III BOSS galaxies*, *Phys. Rev. D* **108** (2023) 083533 [`2302.02925`].

[43] T. Matsubara, *Integrated perturbation theory for cosmological tensor fields. III. Projection effects*, *Phys. Rev. D* **110** (2024) 063545 [`2304.13304`].

[44] T. Okumura, *Evidence for Intrinsic Galaxy Alignments in Ellipticity Autocorrelations out to $100h^{-1}Mpc$ from SDSS Galaxies with DESI Imaging*, `2507.09756`.

[45] F. Schmidt, E. Pajer and M. Zaldarriaga, *Large-Scale Structure and Gravitational Waves III: Tidal Effects*, *Phys. Rev. D* **89** (2014) 083507 [`1312.5616`].

[46] N. Kaiser and A.H. Jaffe, *Bending of light by gravity waves*, *Astrophys. J.* **484** (1997) 545 [`astro-ph/9609043`].

[47] S. Dodelson, E. Rozo and A. Stebbins, *Primordial Gravity Waves and Weak Lensing*, *Phys. Rev. Lett.* **91** (2003) 021301 [`astro-ph/0301177`].

[48] A. Cooray, M. Kamionkowski and R.R. Caldwell, *Cosmic shear of the microwave background: The Curl diagnostic*, *Phys. Rev. D* **71** (2005) 123527 [`astro-ph/0503002`].

[49] J. Yoo, A.L. Fitzpatrick and M. Zaldarriaga, *A New Perspective on Galaxy Clustering as a Cosmological Probe: General Relativistic Effects*, *Phys. Rev. D* **80** (2009) 083514 [`0907.0707`].

[50] S. Dodelson, *Cross-Correlating Probes of Primordial Gravitational Waves*, *Phys. Rev. D* **82** (2010) 023522 [`1001.5012`].

[51] K.W. Masui and U.-L. Pen, *Primordial gravity wave fossils and their use in testing inflation*, *Phys. Rev. Lett.* **105** (2010) 161302 [`1006.4181`].

[52] F. Schmidt and D. Jeong, *Cosmic Rulers*, *Phys. Rev. D* **86** (2012) 083527 [`1204.3625`].

[53] D. Jeong and F. Schmidt, *Large-Scale Structure with Gravitational Waves I: Galaxy Clustering*, *Phys. Rev. D* **86** (2012) 083512 [`1205.1512`].

[54] F. Schmidt and D. Jeong, *Large-Scale Structure with Gravitational Waves II: Shear*, *Phys. Rev. D* **86** (2012) 083513 [`1205.1514`].

[55] N.E. Chisari, C. Dvorkin and F. Schmidt, *Can weak lensing surveys confirm BICEP2?*, *Phys. Rev. D* **90** (2014) 043527 [`1406.4871`].

[56] M. Biagetti and G. Orlando, *Primordial Gravitational Waves from Galaxy Intrinsic Alignments*, *JCAP* **07** (2020) 005 [`2001.05930`].

[57] K. Akitsu, Y. Li and T. Okumura, *Gravitational wave fossils in nonlinear regime: Halo tidal bias and intrinsic alignments from gravitational wave separate universe simulations*, *Phys. Rev. D* **107** (2023) 063531 [`2209.06226`].

[58] O.H.E. Philcox, M.J. König, S. Alexander and D.N. Spergel, *What can galaxy shapes tell us about physics beyond the standard model?*, *Phys. Rev. D* **109** (2024) 063541 [`2309.08653`].

[59] S. Saga, M. Shiraishi, K. Akitsu and T. Okumura, *Imprints of primordial magnetic fields on intrinsic alignments of galaxies*, *Phys. Rev. D* **109** (2024) 043520 [`2312.16316`].

[60] T. Okumura and M. Sasaki, *Extracting parity-violating gravitational waves from projected tidal force tensor in three dimensions*, *JCAP* **10** (2024) 060 [`2405.04210`].

[61] D.M. Eardley, D.L. Lee, A.P. Lightman, R.V. Wagoner and C.M. Will, *Gravitational-wave observations as a tool for testing relativistic gravity*, *Phys. Rev. Lett.* **30** (1973) 884.

[62] D.M. Eardley, D.L. Lee and A.P. Lightman, *Gravitational-wave observations as a tool for testing relativistic gravity*, *Phys. Rev. D* **8** (1973) 3308.

[63] R.w. Hellings and G.s. Downs, *Upper limits on the isotropic gravitational radiation background from pulsar timing analysisS*, *Astrophys. J. Lett.* **265** (1983) L39.

[64] NANOGᴿᴀᴠ collaboration, *The NANOGrav 15 yr Data Set: Search for Transverse Polarization Modes in the Gravitational-wave Background*, *Astrophys. J. Lett.* **964** (2024) L14 [`2310.12138`].

[65] Q. Liang, M.-X. Lin and M. Trodden, *A test of gravity with Pulsar Timing Arrays*, *JCAP* **11** (2023) 042 [`2304.02640`].

[66] Q. Liang, I. Obata and M. Sasaki, *Testing gravity with frequency-dependent overlap reduction function in Pulsar Timing Array*, *JCAP* **10** (2024) 097 [`2405.11755`].

[67] N. Cordes, A. Mitridate, K. Schmitz, T. Schröder and K. Wassner, *On the overlap reduction function of pulsar timing array searches for gravitational waves in modified gravity*, *Class. Quant. Grav.* **42** (2025) 015003 [`2407.04464`].

[68] W. Hu, Q. Liang, M.-X. Lin and M. Trodden, *Testing gravity with realistic gravitational waveforms in Pulsar Timing Arrays*, *JCAP* **12** (2024) 054 [`2408.11774`].

[69] H. Takeda, A. Nishizawa, Y. Michimura, K. Nagano, K. Komori, M. Ando et al., *Polarization test of gravitational waves from compact binary coalescences*, *Phys. Rev. D* **98** (2018) 022008 [1806.02182].

[70] B. Allen, E.E. Flanagan and M.A. Papa, *Is the squeezing of relic gravitational waves produced by inflation detectable?*, *Phys. Rev. D* **61** (2000) 024024 [gr-qc/9906054].

[71] A. Margalit, C.R. Contaldi and M. Pieroni, *Phase decoherence of gravitational wave backgrounds*, *Phys. Rev. D* **102** (2020) 083506 [2004.01727].

[72] D.M. Goldberg and D.J. Bacon, *Galaxy-galaxy flexion: Weak lensing to second order*, *Astrophys. J.* **619** (2005) 741 [astro-ph/0406376].

[73] LIGO SCIENTIFIC, VIRGO, FERMI-GBM, INTEGRAL collaboration, *Gravitational Waves and Gamma-rays from a Binary Neutron Star Merger: GW170817 and GRB 170817A*, *Astrophys. J. Lett.* **848** (2017) L13 [1710.05834].